Langmuir

Article

pubs.acs.org/Langmuir

Elastometry of Deflated Capsules: Elastic Moduli from Shape and Wrinkle Analysis

Sebastian Knoche,[†] Dominic Vella,[‡] Elodie Aumaitre,[§] Patrick Degen,[∥] Heinz Rehage,[∥] Pietro Cicuta,[§] and Jan Kierfeld*,[†]

[†]Department of Physics, Technische Universität Dortmund, 44221 Dortmund, Germany

[‡]Mathematical Institute, Radcliffe Observatory Quarter, Woodstock Road, Oxford OX2 6GG, United Kingdom

[§]Cavendish Laboratory, University of Cambridge, JJ Thomson Avenue, Cambridge CB3 0HE, United Kingdom

[∥]Department of Chemistry, Technische Universität Dortmund, 44221 Dortmund, Germany

Supporting Information

ABSTRACT: Elastic capsules, prepared from droplets or bubbles attached to a capillary (as in a pendant drop tensiometer), can be deflated by suction through the capillary. We study this deflation and show that a combined analysis of the shape and wrinkling characteristics enables us to determine the elastic properties in situ. Shape contours are analyzed and fitted using shape equations derived from nonlinear membrane-shell theory to give the elastic modulus, Poisson ratio and stress distribution of the membrane. We include wrinkles, which generically form upon deflation, within the shape analysis. Measuring the wavelength of wrinkles and using the calculated stress distribution gives the bending stiffness of the membrane. We compare this method with previous approaches using the Laplace−Young equation and illustrate the method on two very different capsule materials: polymerized octadecyltrichlorosilane (OTS) capsules and hydrophobin (HFBII) coated bubbles. Our results are in agreement with the available rheological data. For hydrophobin coated bubbles, the method reveals an interesting nonlinear behavior consistent with the hydrophobin molecules having a rigid core surrounded by a softer shell.

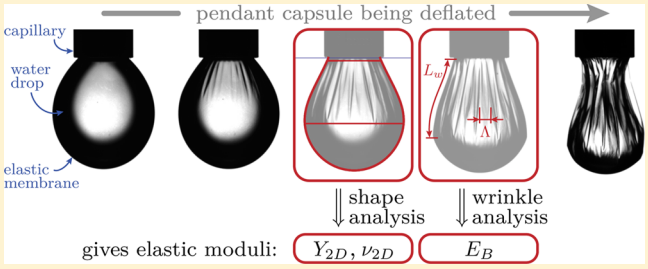

INTRODUCTION

Elastic capsules are ubiquitous in nature as red blood cells, bacterial or virus capsids, while synthetic capsules play an important role in numerous technological applications, including drug delivery and release systems. For stability and applications, the elastic properties of the capsules are crucial, and techniques for the mechanical characterization of single capsules have received much attention (see refs 1 and 2 for recent reviews). Most often, these methods involve contact between the capsule and a probe such as an AFM tip (e.g., refs 3−5). However, only very few noncontact techniques are available, and those that are require motion in a surrounding fluid (e.g., shape analysis in shear flow[6] and spinning drop rheometry[7]).

Synthetic capsules can be fabricated by various methods,[8] many of which are based on reactions at interfaces such as polymerization or the adsorption of surfactants.[9] The latter techniques can be applied to enclose a drop or bubble emerging from a capillary within an elastic membrane. A pendant capsule produced in this way can then be deformed by suction through the capillary in order to analyze its elastic response. Because of the simplicity of this procedure, various membrane materials have been studied in this geometry.[10−13] The analysis of those experiments, however, used models developed for pendant drop tensiometry, a technique widely used to determine the surface tension of *liquid−liquid interfaces* by fitting the drop shape to that predicted by the Laplace−Young equation.[14] This technique is not valid for elastic capsules, since it neglects the elastic stresses within the membrane.[15,16]

In this Article, we present a noncontact elastometry method for individual capsules, inspired by the pendant drop method but adjusting the theoretical model to account for elasticity. Elastic capsules that are attached to a capillary are deflated by sucking some of the enclosed medium back into the capillary. We describe deflated shapes (see Figure 1 for examples) using shell theory for axisymmetric membranes and accounting for the wrinkling induced by deflation. By analyzing the capsule's shape and wrinkling pattern, we can determine its elastic properties, namely, the surface Young modulus, Y_{2D}, describing the membrane's resistance to stretching, and the Poisson ratio ν_{2D} describing the lateral contraction upon stretching. By adjusting these parameters, the theoretical capsule contour can be fitted to the observed shape (Figure 1a and b), and the elastic moduli of the membrane can be determined over a whole range of capsule volumes.

Received: June 19, 2013
Revised: September 6, 2013
Published: September 9, 2013

   dx.doi.org/10.1021/la402322g | *Langmuir* 2013, 29, 12463−12471

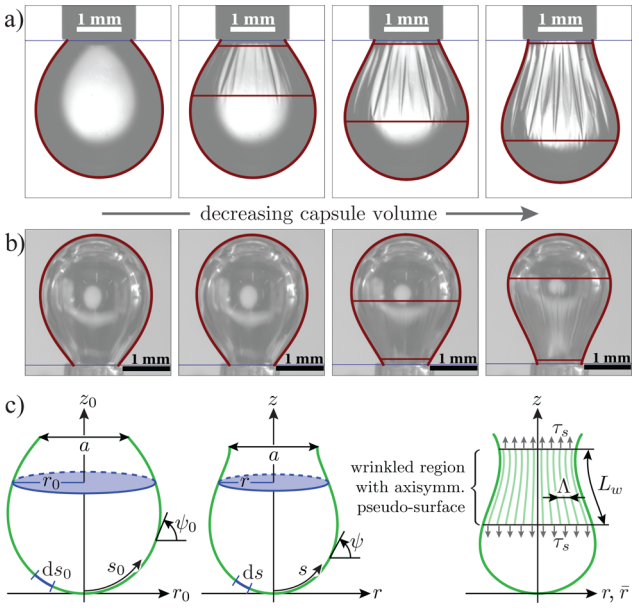

Figure 1. (a, b) Comparison between fitted contour (solid curve) and original image for OTS (a) and HFBII (b) capsules. The first image shows the equilibrated capsule, while the next three show increasing levels of deflation. The extent of the wrinkled region predicted by the model is shown by the horizontal lines. (c) Arc-length parametrizations in cylindrical coordinates of the undeformed ($r_0(s_0)$, $z_0(s_0)$), deformed ($r(s)$, $z(s)$) and wrinkled midsurface (from left to right).

The determination of the membrane's bending stiffness E_B represents another challenge for elastic capsules because it only has a small influence on the capsule contour on large scales and, thus, cannot be obtained by the fitting. Therefore, we combine the shape analysis described above with an analysis of the wrinkles that generically form during deflation, and deduce the bending stiffness from the wavelength of the wrinkles.[17] This combined approach enables us to determine all elastic constants of individual capsules in situ from images of the initial and deflated capsule, thus offering a valuable alternative to rheology in planar geometries. In particular, the capsules studied here have a geometry similar to that of capsules used in applications in pharmacy or industry.

MATERIALS AND METHODS

Elastic Model. We model the capsule as an elastic membrane covering a droplet or bubble, which is attached to a capillary of diameter a. We neglect the bending resistance for simplicity. The axisymmetric reference configuration (Figure 1c, left) is assumed to be free of elastic stresses; the capsule shape is determined by the balance between an isotropic interfacial tension γ and gravity, which is described by the Laplace–Young equation.[18] We make this assumption because the elastic capsule is formed in this initial state from a fluid interface. In the undeformed state, gravity causes the capsule to form the tear drop shape seen in Figure 1. In the absence of gravity, it is well-known that the capsule would take the shape of a spherical cap; we therefore incorporate gravity in our analysis.

Upon deflation, the capsule changes to a deformed configuration, which we assume is axisymmetric (Figure 1c, middle). The local deformation is measured by the meridional and hoop stretches given by

$$\lambda_s = ds/ds_0 \quad \text{and} \quad \lambda_\phi = r/r_0 \tag{1}$$

respectively (see Figure 1c). They lead to elastic tensions according to a Hookean constitutive relation,[19,20] which reads for the meridional tension

$$\tau_s = \frac{Y_{2D}}{1-\nu_{2D}^2}\frac{1}{\lambda_\phi}[(\lambda_s - 1) + \nu_{2D}(\lambda_\phi - 1)] + \gamma \tag{2}$$

with the surface Young modulus Y_{2D} (which for isotropic media is related to the bulk Young modulus Y_{3D} and membrane thickness H_0 by $Y_{2D} = Y_{3D}H_0$) and surface Poisson ratio ν_{2D}. The surface (two-dimensional) Poisson ratio is, for stability reasons, limited to the range $-1 < \nu_{2D} < 1$, as opposed to the bulk (three-dimensional) Poisson ratio which is confined to the range $-1 < \nu_{3D} < 1/2$.[18,21] The constitutive law for the hoop tension τ_ϕ is obtained by interchanging all indices s and ϕ. An equilibrium capsule configuration has to satisfy the force balance equations[19]

$$0 = -\frac{\cos\psi}{r}\tau_\phi + \frac{1}{r}\frac{d(r\tau_s)}{ds}$$
$$p - \Delta\rho g z = \kappa_\phi\tau_\phi + \kappa_s\tau_s \tag{3}$$

Here, p is the pressure inside the capsule at the apex and $\Delta\rho\, g\, z$ is the pressure contribution caused by gravity and the density difference between the inner and outer fluids. The principal curvatures are denoted by κ_s and κ_ϕ, and the slope angle ψ is defined in Figure 1c. This system of differential equations must be solved numerically subject to boundary conditions that fix the capsule radius to the inner radius of the capillary, $a/2$, and ensure that the capsule is closed and smooth at its apex. Using these boundary conditions, eq 3 determines the capsule shape (and, therefore, also the capsule volume V) for given material parameters Y_{2D} and ν_{2D} and given pressure p. More details are given in Appendix I.

If the capsule is deflated sufficiently, regions with compressive hoop stress (i.e., $\tau_\phi < 0$) develop and wrinkles form in order to release this stress, which a membrane with small bending modulus cannot support.[22−25] For fully developed wrinkles, the hoop stress is almost completely relaxed,[22] and so we modify the shape equations by setting $\tau_\phi = 0$ in the wrinkled region. Assuming wrinkles of small amplitude, the membrane can be described by an axisymmetric pseudosurface with radial coordinate $\bar{r}(s)$ around which the wrinkled non-axisymmetric midsurface oscillates;[19] see also Appendix I. Using the condition $\tau_\phi = 0$ in eq 2 to find $\lambda_\phi(\lambda_s)$ we then obtain a modified expression for τ_s in the wrinkled region in terms of λ_s, in which λ_ϕ is eliminated. This allows us to obtain a closed set of modified shape equations in the wrinkled region by applying the axisymmetric force balance (eq 3) to the pseudosurface. Theoretical axisymmetric shapes obtained from integrating eq 3 can then be fitted to experimental images by varying the two material parameters Y_{2D} and ν_{2D} and the pressure p.

We have not included a bending energy in the model described above because, for thin membranes with a small bending modulus ($E_B \propto Y_{2D}H_0^2$ in the case of isotropic materials), the bending moments give only small corrections in the shape equations (eq 3). These corrections are controlled by the dimensionless parameter $E_B/\gamma a^2$. Using $a \sim 1$ mm as the capillary diameter, we find that this parameter is only of the order of 10^{-6} for OTS and 10^{-10} for HFBII capsules. Therefore, E_B cannot be inferred directly from an analysis of the capsule's shape.

Wrinkle Wavelength. The shape equations can predict the regions where wrinkles will occur, but not their amplitude and wavelength. These characteristics are mainly determined by the bending modulus E_B of the membrane.

As shown in Figure 2, the wrinkled region is curved in both meridional and circumferential direction with curvatures $\kappa_s = 1/R_s$ and $\kappa_\phi = 1/R_\phi$, which we assume to be approximately constant. Within this region, we assume a homogeneous state of stress with tensional $\tau_s > 0$ and (without wrinkling) compressive $\tau_\phi < 0$. The wavelength of the wrinkles can be determined by balancing the main contributions to the deformation energy: bending in the circumferential direction and stretching in both circumferential and meridional directions. Changes

dx.doi.org/10.1021/la402322g | Langmuir 2013, 29, 12463−12471

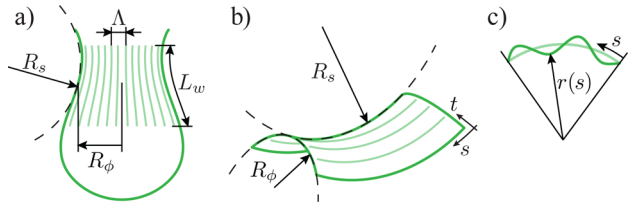

Figure 2. (a) The wrinkled region of a capsule is curved in the meridional and circumferential directions. (b) Geometry for the analytic calculation of the deformation energies. The membrane patch has two radii of curvature, R_s and R_ϕ, and is parametrized via the arc lengths s (in meridional direction) and $t = \phi R_\phi$ (in circumferential direction). (c) An initially curved fiber (in either s or t direction) is wrinkled by adding a sinusoidal normal displacement.

in the gravitational potential energy caused by wrinkling are neglected since the wrinkles are largely parallel to the z-axis.

Upon wrinkling, the membrane is displaced sinusoidally in the normal direction resulting in local strains $\varepsilon_s = |\partial r/\partial s| - 1$ and $\varepsilon_\phi = |\partial r/\partial t| - 1$ (see Figure 2). As they are working against the meridional and circumferential tension, respectively, the stretching energy during the formation of wrinkles is

$$W_S = \int \mathrm{d}s\, \mathrm{d}t\{\tau_s\varepsilon_s + \tau_\phi\varepsilon_\phi\} \tag{4}$$

The bending energy is mainly determined by the curvature change $\Delta\kappa_\phi$ in the circumferential direction and reads

$$W_B = \int \mathrm{d}s\, \mathrm{d}t\left\{\frac{1}{2}E_B(\Delta\kappa_\phi)^2\right\} \tag{5}$$

The evaluation of these integrals is performed in Appendix II. Wrinkling occurs because of a competition between the increase in elastic energy caused by bending and meridional stretching and the decrease in energy achieved by releasing the compressive stress τ_ϕ. The wrinkled state becomes energetically preferable if $W_S + W_B < 0$, corresponding to (see Appendix II)

$$\tau_\phi < -\tau_s\frac{\Lambda^2}{4L_w^2} - E_B\frac{\Lambda^2}{4\pi^2}\left(\frac{4\pi^2}{\Lambda^2} - \frac{1}{R_\phi^2}\right)^2 \tag{6}$$

where L_w is the length of the wrinkles and Λ their wavelength; see Figure 2a.

The first wrinkling mode to be observed has a wavelength Λ_c that minimizes $|\tau_\phi(\Lambda)|$,

$$\Lambda_c = \left(\frac{16\pi^2E_BL_w^2}{\tau_s + E_BL_w^2/\pi^2R_\phi^4}\right)^{1/4} \approx \left(\frac{16\pi^2E_BL_w^2}{\tau_s}\right)^{1/4} \tag{7}$$

The final approximation holds if $R_\phi \gg \Lambda$, which is clearly the case in the experiments presented here (see Figure 1). The approximated form agrees with the results of ref 17 for a planar geometry.

Fitting Procedure. Based on the theory presented above, a three step fitting procedure can be used in order to determine the elastic moduli of the capsule membrane:

(1) The undeformed capsule shape is fitted using the Laplace–Young equation with the interfacial tension γ and pressure p_0 inside the capsule as free parameters.

(2) Shape analysis: Solutions of the shape eqs 3 are fitted to images of the capsule with p, ν_{2D}, and $K_{2D} = Y_{2D}/2(1 - \nu_{2D})$ (area compression modulus) as free parameters at each stage of deflation.

(3) Wrinkle analysis: The wavelength Λ in the center of the wrinkled region is measured from images. The length L_w of the wrinkles and a mean value of τ_s over this region are obtained from the fitted solution. Then, the bending modulus E_B is determined from eq 7 (or eq 29, see Appendix II). Using the relationship $E_B = Y_{2D}H_0^2/12(1 - \nu_{3D}^2)$ from classical shell theory,[26] an effective membrane thickness H_0 can also be estimated[27]

Note that the position and height L_w of the wrinkled region are *not* fit parameters but can be used as an independent check of the goodness of the fit. Technical details of the fitting procedure and the underlying image analysis are contained in the Supporting Information. L_w is determined from the fitted numerical solution as the arc length over which the modified shape equations (with $\tau_\phi = 0$) were integrated, see the Appendix I.

We now demonstrate this method on two rather different types of capsules: polymerized OTS capsules and bubbles coated with an interfacial monolayer film of the protein hydrophobin.

Preparation of Capsules. To prepare a pendant capsule, a glass cell is filled with p-xylene containing OTS. Then a drop of water is placed into this phase using a syringe. The polymerization process starts immediately after the oil/water interface is formed. Hydrophobin coated bubbles are prepared in a very similar fashion. As described in previous work,[28] an air bubble is placed into a solution of HFBII in water using a J-shaped needle and HFBII molecules adsorb at the interface over the course of 20 min.

After equilibration, the capsules are deflated slowly (i.e., quasi-statically, on a time scale of ~10 s for a deflation of OTS capsules and even slower for HFBII capsules) by sucking the enclosed medium back into the syringe. The OTS capsule is subsequently reinflated to check whether the deformation is reversible.

EXPERIMENTS AND RESULTS

Test of Shape Analysis. We first test our elastometry approach by applying it to fit numerically generated capsule shapes. To this end, we take an initial capsule configuration (γ = 49.8 mN/m, $\Delta\rho_0$ = 1000 kg/m^3, and V_0 = 8.23 mm^3, values taken from the HFBII capsule) and use our shape equations with fixed elastic moduli (K_{2D} = 600 mN/m, ν_{2D} = 0.3) to compute deflated configurations. From a contour, we calculate a set of approximately 150 sampling points, optionally add some noise to simulate an imperfect contour analysis, and pass them to the fitting procedure to see if it finds the correct solution.

Figure 3 shows that all fits to the clean contour (green triangles) are successful and recover the original compression modulus. The elastic fits to the noisy contour (blue points) succeed if the deformation is large enough, that is, for $V/V_0 \leq$

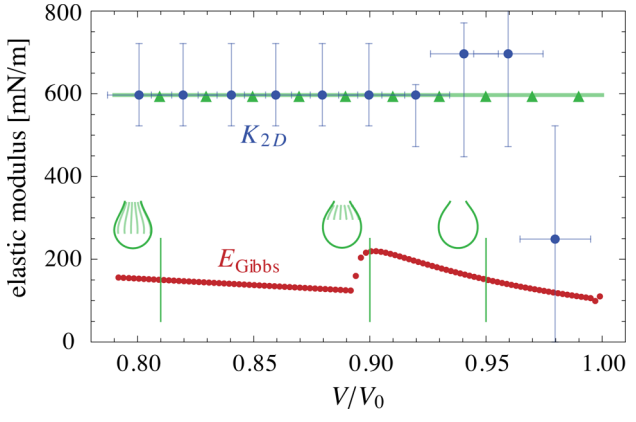

Figure 3. Fit results for theoretically generated capsule shapes with K_{2D} = 600 mN/m (green line). Green triangles represent the fits of the elastic shape equations to the clean contour, blue dots the elastic fits to the noisy contour, and red points the Gibbs elasticity calculated from Laplace–Young fits. Vertical green lines indicate the positions of the capsule pictograms shown in green.

dx.doi.org/10.1021/la402322g | Langmuir 2013, 29, 12463–12471

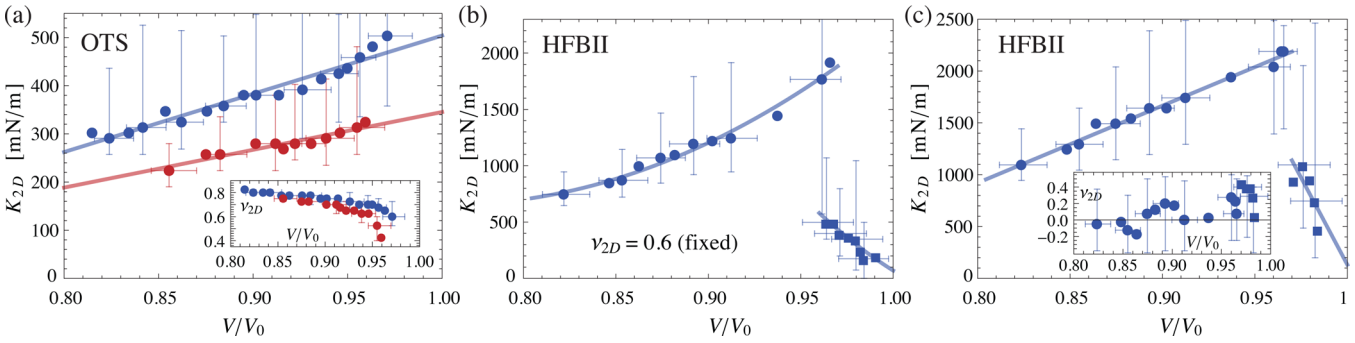

Figure 4. Fit results for (a) an OTS capsule and (b, c) an HFBII capsule, with nonwrinkled (■) and wrinkled (●) shapes. Error bars were generated by displacing the sampling points by about ±1 pixel; see the Supporting Information. Lines are drawn to guide the eye. (a) Upper blue curve is for deflation, and lower red curve for reinflation. The deflation was driven to even smaller volumes than shown, but for these the contour analysis failed. (b) For HFBII, the Poisson ratio was fixed to ν_{2D} = 0.6. (c) The same HFBII capsule fitted with free Poisson ratio.

0.94 in the present case. For smaller deformations, there are some deviations in the fit results, but the error bars are large enough to reach the real value, except for the very first fit (V/V_0 = 0.98). This problem arises due to the very small deformation: The root-mean-square deviation between the initial shape and the shape at V/V_0 = 0.98 is about 0.01 length units, the noise amplitude is 0.005, and the offset used for the error bars is ±0.007 (corresponding to ±1 pixel at usual image resolution). So the sampling points passed to the fitting procedure have an offset from their original place which is of the same order as the deformation; we could not have expected the fits to work.

Comparison to Laplace−Young Analysis. For comparison with our new method, we also consider the performance of the usual Laplace−Young analysis used by many scientists.[10−12] In a Laplace−Young analysis, elastic capsules are fitted with the Laplace−Young equation to obtain the interfacial tension γ and capsule surface A over the course of the deflation; these tools are provided by the software of common pendant drop tensiometers. The Gibbs elastic modulus $E_{Gibbs} = A\, d\gamma/dA$ is often then calculated from these values. In applying this method to theoretically generated capsules shapes, we find that E_{Gibbs} is significantly smaller than the actual area compression modulus; see Figure 3. It appears that for elastic capsules, the intricate interplay between membrane geometry and elastic tensions renders the Laplace−Young analysis more erroneous than intuitively expected: Not even for small deformation does the Gibbs elastic modulus approach the real area compression modulus. This explains the observations of Stanimirova et al. that pendant drop tensiometry gives misleading results if applied to capsules with high surface elasticity.[11]

Fit Results for OTS and HFBII Capsules. For OTS and HFBII capsules, several images of the undeformed reference configurations are fitted to the solution of the Laplace-Young equation. The results are averaged to obtain the surface tension γ = 11.2 mN/m for OTS and γ = 49.8 mN/m for HFBII. Both values are lower than the respective values of the clean interfaces because the OTS and HFBII molecules are surface active agents that lower the interfacial tension during adsorption.

Deflated capsule configurations with varying volume are fitted using the elastic model. Figure 4a shows the results for an OTS capsule. All data points in Figure 4a represent wrinkled shapes, because even the slightest deformation gives rise to wrinkles due to the low initial surface tension and high compression modulus. We find an area compression modulus K_{2D} which decreases with decreasing V/V_0. Although the error bars in Figure 4a are overlapping, this result is reliable because the error bars represent worst case systematic errors (see the Supporting Information). The deformation is not perfectly reversible, and we observe hysteresis: The area compression modulus obtained for reinflated capsules is lower (lower red vs upper blue data points in Figure 4a). The presence of hysteresis indicates that the decreasing modulus is not an artifact of the method but a result of creep, for example, by viscous effects, that is, breakage or rearrangement of bonds in the OTS network, or by the formation of microdefects such as shear cracks. The video in the Supporting Information shows, however, that computed contours with the moduli fixed to the small-deformation values $K_{2D} \approx$ 500 mN/m and $\nu_{2D} \approx 0.6$ are in good agreement with all experimental observations, implying that the nonlinear effects are moderate. The resulting surface shear modulus[21] is $G_{2D} = K_{2D}(1 - \nu_{2D})/(1 + \nu_{2D}) \approx$ 125 mN/m. In ref 9, larger values of 200−300 mN/m (obtained by interfacial shear rheology) are reported for similar OTS membranes. In another experiment with three deflation/inflation cycles of an OTS capsule, we saw that the capsule does not weaken further after the first deflation, but hysteresis was observed in all cycles. The hysteresis may possibly depend on the deflation velocity and may thus contain information about the viscous part of the membrane viscoelasticity, this issue is left for future research. Since all viscous effects have been neglected in the elastic model, our analysis should only be applied to quasi-static experiments.

In the case of HFBII, we can reduce the number of fit parameters by constraining ν_{2D} = 0.6 to a value measured in an independent experiment[29] and determine the area compression modulus only. Figure 4b shows that the area compression modulus K_{2D} increases for small deformations, where the capsule does not wrinkle (blue squares in Figure 4b), to values around 500 mN/m. The onset of wrinkling coincides with a sharp increase of the modulus to a maximum value of $K_{2D} \approx$ 2000 mN/m. This sharp increase is consistent with the molecular structure of HFBII,[30] which contains a rigid core consisting of four β-strands and is stabilized by disulfide bridges. The modulus K_{2D} increases sharply when compression of this rigid protein core sets in, while at small deformations, only contacts between hydrophobin proteins or a soft shell consisting of coil and loop structures surrounding the rigid β-barrel are compressed. The sharp rise of the compression modulus triggers wrinkling. Subsequently, the compression modulus decreases again (blue circles in Figure 4b) likely signaling creep as also observed for the OTS capsules. Possible

dx.doi.org/10.1021/la402322g | Langmuir 2013, 29, 12463−12471

explanations for the creep behavior are the formation of microdefects such as shear cracks or localized bulges into the subphase, which weaken the hydrophobin layer.

The choice of the fixed value for ν_{2D} influences the absolute values obtained for K_{2D} and the size of its jump when wrinkling sets in, while the characteristics described above are robust. Taking the Poisson ratio as a fit parameter also results in a similar course of the elastic modulus; see Figure 4c. And yet the results for ν_{2D} differ substantially from the previously assumed value of $\nu_{2D} = 0.6$. Especially for small deformations, this results in higher values for the area compression modulus.

The values $K_{2D} < 500$ mN/m for the compression modulus for small deformations and prior to wrinkling are in good agreement with values reported previously for HFBII.[12,31,32] The large values around $K_{2D} = 2000$ mN/m at the onset of wrinkling have not been reported before, since the experimental methods used in the literature are not reliable in the presence of wrinkles. However, a comparison to viral capsids consisting of densely packed proteins is possible. In ref 33, the bulk Young modulus of a viral capsid is measured as 1.8 GPa, which is comparable to our result for the bulk modulus $Y_{3D} = Y_{2D}/H_0 \approx 1$ GPa, where $H_0 \approx 2$ nm is the hydrophobin layer thickness.[34]

Analysis of the Wrinkle Wavelength. Finally, the wrinkling pattern shall be analyzed and be related to the bending stiffness. The wavelength of the wrinkles on the HFBII capsules cannot be measured directly: due to the low bending stiffness, the wavelength is too small to be resolved in the experimental images (note that the observable folds in Figure 1b are not primary wrinkles, but rather secondary or higher order structures). However, using eq 7 with L_w, τ_s, and $E_B = Y_{2D}H_0^2/12(1 - \nu_{3D}^2)$ obtained from the elastic fits, we expect wavelengths between 7.6 and 11 μm. In the literature, similarly small or even smaller wrinkle wavelengths for compressed HFBII films in a Langmuir trough have been reported.[24,29,32]

For OTS capsules, however, wrinkle wavelengths Λ may be determined from images. Values for τ_s in the wrinkled region and L_w are taken from the elastic fits and are documented in Figure 5 (dark blue and dark red dots). The resulting bending stiffness is $E_B \approx (2.5 \pm 0.7) \times 10^{-14}$ Nm; that is, 3 orders of magnitude larger than previous estimates[17,35] which used an experiment with a smaller capsule of the same material in shear flow, resulting in wrinkles with a shorter wavelength.[36] Moreover, OTS capsules in ref 36 were prepared in a different aqueous solution (glycerol and NaOH) and using longer polymerization times. These differences can give rise to distinct membrane thicknesses and cross-link densities, which can explain the differences in the bending modulus: the bending modulus varies with the third power of the membrane thickness (Cerda and Mahadevan estimated in ref 17 a thickness around 20 times smaller than that of the capsules used here). Combining this value for E_B with measurements of Y_{2D} from the shape analysis we estimate the membrane thickness $H_0 \approx (0.77 \pm 0.07)$ μm, which is in approximate agreement with capsule thicknesses $0.86 < H_0 < 1.4$ μm measured by electron microscopy; see the Supporting Information. Also the extent and position of the wrinkled region are in good agreement with the experimental data (see Figure 5): Except for the last part of the reinflation curve, the curves for the wrinkle length of the elastic fits (dark symbols) and for the directly measured wrinkle length (light symbols) are quite close to each other.

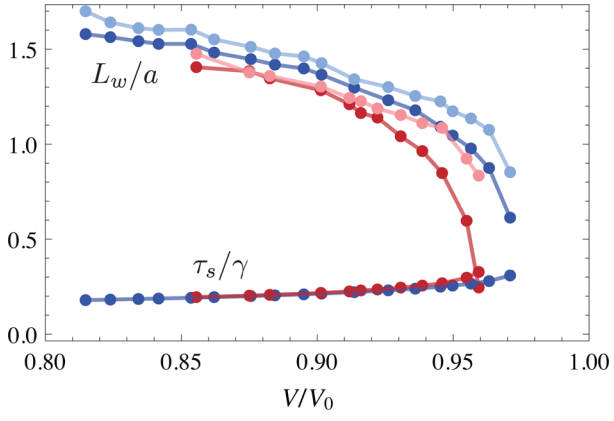

Figure 5. Wrinkle length L_w (upper curves) and mean tension τ_s (lower curves), both in reduced units for the wrinkled OTS capsule; the unit length is $a = 1.44$ mm, and tension unit $\gamma = 11.2$ mN/m. Blue dots indicate the deflation results, and red dots the reinflation. Dark blue and dark red represent results taken from the fitted shape equations, and light blue and light red represent direct measurements from the images.

CONCLUSIONS

The proposed theory for axisymmetric capsule shapes in the presence of wrinkling describes deflated experimental shapes of both OTS capsules and hydrophobin coated bubbles accurately. It is possible to fit the solutions of the shape equations to contours extracted from experimental images in order to find the elastic properties (area compression modulus and Poisson ratio) of the membrane. Additionally, a subsequent analysis of the wavelength of wrinkles which occur during the deflation can determine the membrane's bending stiffness. With this combination of analyses, the elastic properties of the capsule are completely characterized.

Applying this method to OTS capsules gives reasonable values for all three elastic constants: $K_{2D} \approx 500$ mN/m, $\nu_{2D} \approx 0.6$, and $E_B \approx 2.5 \times 10^{-14}$ Nm for the small deformation behavior. Furthermore, we observe a softening or creep of the capsules with decreasing volume, which we also observe for hydrophobin capsules (see Figure 4).

For hydrophobin capsules, the area compression modulus initially grows upon deflation, $K_{2D} = 160$ to 500 mN/m when we assume $\nu_{2D} = 0.6$. At the onset of wrinkling, it jumps to 2000 mN/m because compression of the rigid protein core sets in (see Figure 4b and c). Obviously, this complex behavior cannot be explained by simple Hookean elasticity, and we hope that these results will inspire future work on possible nonlinear elastic laws for HFBII membranes or other membrane materials consisting of hard core particles. According to our observations, this should include an immense strain stiffening upon compression. In the application of the Laplace–Young analysis to elastic capsules, we found that the shape analysis reacts delicately to inaccuracies in the model for the membrane tensions. Likewise, a certain amount of caution is advisable when our elastometry method indicates a strongly nonlinear elasticity, as in the present analysis of the HFBII capsule. In this case, obviously nonlinear elasticity is fitted with a simple Hookean constitutive law, and we cannot be sure which characteristics of the results reflect limitations of the linearly elastic model.

These two applications prove the concept of the elastometry method, which could be added to the features of pendant drop tensiometers in the future. The method can reveal changes in elastic constants with decreasing volume that are not accessible

dx.doi.org/10.1021/la402322g | Langmuir 2013, 29, 12463–12471

by other methods. It can be further improved by using data from a simultaneous pressure measurement during deflation, which would eliminate one of the fit parameters.

APPENDIX I: SHAPE EQUATIONS

The Nonwrinkled Case

In this Appendix, we show how the elastic model, defined in the main text by Figure 1c and eqs 1−3, can be treated numerically. This is best handled when a system of first order differential equations is constructed from the force balance, constitutive, and geometrical equations.

The axisymmetric reference configuration of the pendant or rising capsule is described in cylindrical coordinates by a midsurface parametrization $(r_0(s_0), z_0(s_0))$ with $s_0 \in [0, L_0]$ being the arc length. It is free of elastic tensions; the capsule retains its shape only because of an isotropic interfacial tension γ. Accordingly, the reference shape is described by the Laplace−Young equation[18]

$$\gamma(\kappa_{s0} + \kappa_{\phi 0}) = p_0 - \Delta\rho g z_0 \tag{8}$$

where κ_{s0} and $\kappa_{\phi 0}$ are the principal curvatures and $p_0 - \Delta\rho g z_0$ is the hydrostatic pressure caused by the density difference of inner and outer fluid.

When exerting forces on the capsule, it changes to a deformed configuration $(r(s_0), z(s_0))$, with the so-called "material coordinate" s_0 still running from 0 to L_0. Alternatively, we can choose an arc length parametrization $(r(s), z(s))$ plus a mapping $s(s_0)$ to describe this configuration.

In the latter notation, some geometric relations can be written quite conveniently. For later use, we introduce the slope angle ψ (see Figure 1c) defined by

$$\cos\psi = \mathrm{d}r/\mathrm{d}s \quad \text{and} \quad \sin\psi = \mathrm{d}z/\mathrm{d}s \tag{9}$$

and the principal curvatures

$$\kappa_s = \mathrm{d}\psi/\mathrm{d}s \quad \text{and} \quad \kappa_\phi = \sin\psi/r \tag{10}$$

Together with the force balance (eq 3), strain definition (eq 1) and elastic law (eq 2), these relations can be used to construct a system of first order differential equations with the material coordinate s_0 as variable,

$$\begin{aligned} r'(s_0) &= \lambda_s \cos\psi \\ z'(s_0) &= \lambda_s \sin\psi \\ \psi'(s_0) &= \frac{\lambda_s}{\tau_s}(p - \Delta\rho g z - \kappa_\phi \tau_\phi) \\ \tau_s'(s_0) &= -\lambda_s \cos\psi \frac{\tau_s - \tau_\phi}{r} \end{aligned} \tag{11}$$

All functions occurring on the right-hand side of the system must be expressed in terms of the basic functions r, z, ψ, τ_s via the previously mentioned geometric relations and definitions of stretches and tensions. The boundary conditions are obvious from the geometry of the capsule, $r(0) = z(0) = \psi(0) = 0$ and $r(L_0) = a/2$, where a is the inner diameter of the capillary. Finally, some limits for $s_0 \to 0$ must be evaluated analytically using L'Hôspital's rule to start the integration. For the nondimensionalization, we choose the capillary diameter a as the length unit and the interfacial tension γ of the initial shape as tension unit.

Extending the Model to Wrinkled Shapes

Now we want to calculate wrinkled configurations (with wave vector along the hoop direction). Configurations of this kind arise because ideal membranes without bending resistance cannot support negative tensions. They are not exactly axisymmetric, but can be approximated by an axisymmetric pseudo-surface in the wrinkled region. The shape $(\overline{r}(s_0), \overline{z}(s_0))$ of the pseudosurface is obtained by requiring $\tau_\phi = 0$ in areas where the original model would yield $\tau_\phi < 0$.[19]

According to Hooke's law (eq 2), the wrinkling condition $\tau_\phi < 0$ is equivalent to

$$\lambda_\phi < 1 - \gamma\frac{1 - \nu_{2D}^2}{Y_{2D}}\lambda_s - \nu_{2D}(\lambda_s - 1) \tag{12}$$

At the point where λ_ϕ falls below this threshold during the numeric integration of eq 11, we switch to a modified system of shape equations to continue the integration. This system describes the pseudosurface and is mainly determined by setting $\tau_\phi = 0$ on the wrinkling domain, that is

$$\lambda_\phi = 1 - \gamma\frac{1 - \nu_{2D}^2}{Y_{2D}}\lambda_s - \nu_{2D}(\lambda_s - 1) \tag{13}$$

Note that λ_ϕ is the hoop stretch of the real, wrinkled midsurface and not to be confused with the stretch $\overline{\lambda}_\phi = \overline{r}/r_0$ of the pseudosurface (all quantities referring to the pseudosurface are indicated with an overbar).

In order to eliminate the hoop stretch of the real midsurface from our system of equations, we insert this expression (eq 13) into the constitutive relation (eq 2) for the meridional tension,

$$\tau_s = Y_{2D}\frac{1}{\lambda_\phi}\left[(\lambda_s - 1) - \frac{\nu_{2D}\gamma}{Y_{2D}}\lambda_s\right] + \gamma \tag{14}$$

However, this tension is not suitable for considering the force balance since it is measured per unit length of the wrinkled, non-axisymmetric midsurface. In order to adopt the simple force balance (eq 3) for the pseudosurface, we have to measure the tension per unit length of the pseudosurface, $\overline{\tau}_s = \tau_s\lambda_\phi/\overline{\lambda}_\phi$, resulting in

$$\overline{\tau}_s = \frac{1}{\overline{\lambda}_\phi}\left[\lambda_s\left(Y_{2D} - 2\nu_{2D}\gamma - \gamma^2\frac{1 - \nu_{2D}^2}{Y_{2D}}\right) - Y_{2D} + \gamma(1 + \nu_{2D})\right] \tag{15}$$

With this constitutive equation for $\overline{\tau}_s$ and $\overline{\tau}_\phi = 0$ and all geometric relations adopted to the pseudosurface, the modified shape equations for the wrinkled part are established.

Numerical Integration with Automatic Switching between the Shape Equations in Wrinkled Regions

The shape equations are integrated numerically using a shooting method with $\tau_s(0)$ as the free shooting parameter, which is adjusted until the boundary condition $r(L_0) = a/2$ at the far end is satisfied.

The integration starts at the apex, using the usual shape eqs 11. In each integration step, the wrinkling condition (eq 12) is checked. When λ_ϕ falls below this threshold, at $s_0 = s_A$, the integration is stopped. From this point on, the wrinkled shape equations are integrated, using continuity conditions for all functions as starting conditions. The integration goes on until

dx.doi.org/10.1021/la402322g | Langmuir 2013, 29, 12463−12471

the point $s_0 = s_B$, where the wrinkling condition is not met any more, that is, where

$$\frac{\bar{r}}{r_0} > 1 - \gamma\frac{1-\nu_{2D}{}^2}{Y_{2D}}\lambda_s - \nu_{2D}(\lambda_s - 1) \tag{16}$$

Then we switch back to the original shape eqs 11, again using continuity conditions for all functions. This last part should run up to the end $s_0 = L_0$, where the boundary deviation $r(L_0) - a/2$ can be calculated. The initial guess of $\tau_s(0)$ at the very beginning of the integration is then adjusted, and after some iterations the boundary deviation should become close to zero. The wrinkle length L_w, necessary for the wrinkling analysis, can be obtained as $L_w = s_B - s_A$.

In some cases, especially for high values of Y_{2D}, a simple shooting method will fail to converge. It turned out that these cases are reliably handled by a multiple shooting method.[37]

APPENDIX II: WAVELENGTH OF THE WRINKLES

We investigate the wrinkling of a surface that is curved in two directions (see Figure 2b) with two different average curvatures $\kappa_s = 1/R_s$ and $\kappa_\phi = 1/R_\phi$ which are constant within the wrinkling region. The region is parametrized by the arc lengths s and $t = \phi R_\phi$. Upon wrinkling, the normal displacement of the surface leads to stretching in both directions, and to bending predominantly in the t-direction because the wavelength Λ in the t-direction is much smaller than that in the s-direction, where we assume only one half sine period. By balancing these main contributions to the deformation energy, we can determine the wrinkling wavelength and critical compressive stress.

The length change of a curved fibre which is displaced sinusoidally in normal direction can be calculated from a parametrization

$$\mathbf{r}(s) = [R + C\sin ks]\begin{pmatrix}\cos s/R\\ \sin s/R\end{pmatrix} \tag{17}$$

up to quadratic order in the wrinkle amplitude C as

$$\varepsilon = \left|\frac{d\mathbf{r}}{ds}\right| - 1 = \frac{C}{R}\sin ks + \frac{1}{2}C^2k^2\cos^2 ks + O(C^3). \tag{18}$$

For the stretching energy in the meridional direction, we assume that the wrinkles have length L_w and hence wave vector $k = \pi/L_w$ in the s-direction. The amplitude of the wrinkles depends on the position along the circumferential direction according to $C(t) = C_0 \sin 2\pi t/\Lambda$, and we take $R = R_s$ in eq 18 to obtain the strain

$$\varepsilon_s(s,t) = \frac{C(t)}{R_s}\sin\frac{\pi s}{L_w} + \frac{\pi^2 C(t)^2}{2L_w{}^2}\cos^2\frac{\pi s}{L_w} \tag{19}$$

Upon wrinkling, this strain has to work against the tension τ_s, resulting in a deformation energy

$$W_s = \int \tau_s\varepsilon_s\, ds\, dt = \pi^3 C_0{}^2 R_\phi \tau_s/4L_w \tag{20}$$

where the tension τ_s was assumed to be constant on the whole integration domain $s \in [0, L_w]$ and $t \in [0, 2\pi R_\phi)$ and the t-range is a multiple of Λ so that the t integration is performed over full sine periods.

The stretch energy in circumferential direction can be calculated analogously, but with wavevector $k = 2\pi/\Lambda$, $R = R_\phi$, and amplitude $C(s) = C_0 \sin(\pi s/L_w)$ used in eq 18, and reads

$$W_\phi = \int \tau_\phi\varepsilon_\phi\, ds\, dt = \pi^3 C_0{}^2 L_w R_\phi \tau_\phi/\Lambda^2 \tag{21}$$

Since $\tau_\phi < 0$, this contribution is negative; that is, it is the energy gain which drives the wrinkling.

The bending is strongest in ϕ-direction, and its energy cost depends on the curvature change of a circumferential fiber. For a curve given in polar coordinates, $r(\phi) = R_\phi + C\sin 2\pi\phi R_\phi/\Lambda$, the curvature can be approximated to first order in the amplitude C as

$$\kappa_\phi \approx \frac{1}{r(\phi)} - \frac{r''(\phi)}{r(\phi)^2} \tag{22}$$

$$\approx \frac{1}{R_\phi} + C\left(-\frac{1}{R_\phi{}^2} + \frac{4\pi^2}{\Lambda^2}\right)\sin\frac{2\pi t}{\Lambda} \tag{23}$$

Considering that the wrinkle amplitude depends on the position along the meridional direction via $C(s) = C_0 \sin \pi s/L_w$, the bending energy reads

$$W_B = \int ds\, dt\left\{\frac{1}{2}E_B\left(\kappa_\phi - \frac{1}{R_\phi}\right)^2\right\} \tag{24}$$

$$= \frac{1}{4}\pi E_B C_0{}^2 L_w R_\phi\left(\frac{4\pi^2}{\Lambda^2} - \frac{1}{R_\phi}\right)^2 \tag{25}$$

For the wrinkled state to become preferable to the unwrinkled state, the total deformation energy $W_s + W_\phi + W_B$ must be negative,

$$\tau_s\frac{\pi^2}{L_w{}^2} + \tau_\phi\frac{4\pi^2}{\Lambda^2} + E_B\left(\frac{4\pi^2}{\Lambda^2} - \frac{1}{R_\phi{}^2}\right)^2 < 0 \tag{26}$$

This condition is equivalent to eq 6 in the main text, repeated here for convenience:

$$\tau_\phi(\Lambda) = -\tau_s\frac{\Lambda^2}{4L_w{}^2} - E_B\frac{\Lambda^2}{4\pi^2}\left(\frac{4\pi^2}{\Lambda^2} - \frac{1}{R_\phi{}^2}\right)^2 \tag{27}$$

The wrinkling will first occur with a wavelength that renders $|\tau_\phi(\Lambda)|$ minimal, which is

$$\Lambda_c = \left(\frac{16\pi^2 E_B L_w{}^2}{\tau_s + E_B L_w{}^2/\pi^2 R_\phi{}^4}\right)^{1/4} \tag{28}$$

Solving this equation for E_B yields

$$E_B = \frac{\tau_s\Lambda^4}{16\pi^2 L_w{}^2(1 - \Lambda^4/16\pi^4 R_\phi{}^4)} \tag{29}$$

which can be used to determine the bending modulus from measurements of the wrinkle wavelength.

If the wrinkle wavelength is much smaller than the radius of curvature, $\Lambda \ll R_\phi$, the term $1/R_\phi{}^2$ in eq 27 can be neglected and the resulting critical wavelength is exactly the result of Cerda and Mahadevan,[17]

dx.doi.org/10.1021/la402322g | Langmuir 2013, 29, 12463−12471

$$\Lambda_c = \left(\frac{16\pi^2 E_B {L_w}^2}{\tau_s} \right)^{1/4} \tag{30}$$

Note that the small ratio Λ/R_ϕ enters the formula for E_B (eq 29) in the fourth power, so that the influence of the initial curvature of the membrane has only little influence on the wavelength analysis, and can therefore be neglected.

For the shape equations in the wrinkled region, this compressive circumferential stress is set to zero. That can be justified by considering its order of magnitude: The compressive stress for the critical wavelength reads (in the limit $\Lambda \ll R_\phi$, for simplicity)

$$\tau_{\phi,c} = \tau_\phi(\Lambda_c) = -\sqrt{\frac{4\pi^2 E_B \tau_s}{{L_w}^2}} \tag{31}$$

Estimating $E_B \sim E_{2D}{H_0}^2$ by the relation from classical shell theory and $\tau_s \sim \gamma$ leads to a dimensionless parameter

$$\frac{|\tau_{\phi,c}|}{\gamma} \sim \sqrt{\frac{E_{2D}}{\gamma}} \frac{H_0}{L_w} \tag{32}$$

Whereas the membrane thickness H_0 is of the order of micro- to nanometers, the wrinkle length is around 1 mm. Thus, the nondimensionalized critical compression is only of the order 10^{-6}–10^{-3}.

■ ASSOCIATED CONTENT

Supporting Information

Technical details on the image analysis and fitting procedure. Video of the OTS experiment and fitted shape equations (green line, with K_{2D} = 500 mN/m and ν_{2D} = 0.6 fixed); the blue lines indicate the computed amplitude of the wrinkles. This material is available free of charge via the Internet at http://pubs.acs.org/.

■ AUTHOR INFORMATION

Corresponding Author

*E-mail: jan.kierfeld@tu-dortmund.de.

Notes

The authors declare no competing financial interest.

■ ACKNOWLEDGMENTS

S.K. and J.K. acknowledge financial support by the Mercator Research Center Ruhr (MERCUR). D.V. is partially supported by a Leverhulme Trust Research Fellowship. E.A. and P.C. thank Unilever Global Development Centre for the gift of hydrophobin and EPSRC and Unilever, plc for funding.

■ REFERENCES

(1) Fery, A.; Weinkamer, R. Mechanical properties of micro- and nanocapsules: Single- capsule measurements. *Polymer* **2007**, *48*, 7221–7235.

(2) Li, B.; Cao, Y.-P.; Feng, X.-Q.; Gao, H. Mechanics of morphological instabilities and surface wrinkling in soft materials: a review. *Soft Matter* **2012**, *8*, 5728.

(3) Gordon, V. D.; Chen, X.; Hutchinson, J. W.; Bausch, A. R.; Marquez, M.; Weitz, D. a. Self-assembled polymer membrane capsules inflated by osmotic pressure. *J. Am. Chem. Soc.* **2004**, *126*, 14117–14122.

(4) Arfsten, J.; Leupold, S.; Bradtmöller, C.; Kampen, I.; Kwade, A. Atomic force microscopy studies on the nanomechanical properties of Saccharomyces cerevisiae. *Colloids Surf., B* **2010**, *79*, 284–290.

(5) Vella, D.; Ajdari, A.; Vaziri, A.; Boudaoud, A. The indentation of pressurized elastic shells: from polymeric capsules to yeast cells. *J. R. Soc., Interface* **2012**, *9*, 448–455.

(6) Chang, K. S.; Olbricht, W. L. Experimental studies of the deformation and breakup of a synthetic capsule in steady and unsteady simple shear flow. *J. Fluid. Mech.* **1993**, *250*, 609–633.

(7) Pieper, G.; Rehage, H.; Barthès-Biesel, D. Deformation of a Capsule in a Spinning Drop Apparatus. *J. Colloid Interface Sci.* **1998**, *202*, 293–300.

(8) Meier, W. Polymer nanocapsules. Chem. *Soc. Rev.* **2000**, *29*, 295–303.

(9) Rehage, H.; Husmann, M.; Walter, A. From two dimensional model networks to microcapsules. *Rheol. Acta* **2002**, *41*, 292–306.

(10) Husmann, M. Polyorganosiloxan-Filme zwischen fluiden Phasen. Ph.D. Thesis, Universität Essen, 2001.

(11) Stanimirova, R.; Marinova, K.; Tcholakova, S.; Denkov, N. D.; Stoyanov, S. D.; Pelan, E. Surface rheology of saponin adsorption layers. *Langmuir* **2011**, *27*, 12486–98.

(12) Alexandrov, N. A.; Marinova, K. G.; Gurkov, T. D.; Danov, K. D.; Kralchevsky, P. A.; Stoyanov, S. D.; Blijdenstein, T. B.; Arnaudov, L. N.; Pelan, E. G.; Lips, A. Interfacial Layers from the Protein HFBII Hydrophobin: Dynamic Surface Tension, Dilatational Elasticity and Relaxation Times. *J. Colloid Interface Sci.* **2012**, *376*, 296–306.

(13) Erni, P.; Jerri, H. A.; Wong, K.; Parker, A. Interfacial viscoelasticity controls buckling, wrinkling and arrest in emulsion drops undergoing mass transfer. *Soft Matter* **2012**, *8*, 6958.

(14) Rotenberg, Y.; Boruvka, L.; Neumann, A. Determination of Surface Tension and Contact Angle from the Shapes of Axisymmetric Fluid Interfaces. *J. Colloid Interface Sci.* **1983**, *93*, 169–183.

(15) Carvajal, D.; Laprade, E. J.; Henderson, K. J.; Shull, K. R. Mechanics of pendant drops and axisymmetric membranes. *Soft Matter* **2011**, *7*, 10508.

(16) Ferri, J. K.; Fernandes, P. a. L.; McRuiz, J. T.; Gambinossi, F. Elastic nanomembrane metrology at fluid-fluid interfaces using axisymmetric drop shape analysis with anisotropic surface tensions: deviations from Young-Laplace equation. *Soft Matter* **2012**, *8*, 10352.

(17) Cerda, E.; Mahadevan, L. Geometry and Physics of Wrinkling. *Phys. Rev. Lett.* **2003**, *90*, 074302.

(18) Landau, L.; Lifshitz, E. *Fluid Mechanics*; Butterworth-Heinemann: Oxford, 1987.

(19) Libai, A.; Simmonds, J. *The Nonlinear Theory of Elastic Shells*; Cambridge University Press: Cambridge, 1998.

(20) Knoche, S.; Kierfeld, J. Buckling of spherical capsules. *Phys. Rev. E* **2011**, *84*, 046608.

(21) Barthès-Biesel, D.; Diaz, A.; Dhenin, E. Effect of constitutive laws for twodimensional membranes on flow-induced capsule deformation. *J. Fluid Mech.* **2002**, *460*, 211–222.

(22) Davidovitch, B.; Schroll, R. D.; Vella, D.; Adda-Bedia, M.; Cerda, E. Prototypical model for tensional wrinkling in thin sheets. *Proc. Natl. Acad. Sci. U.S.A.* **2011**, *108*, 18227–32.

(23) Vella, D.; Ajdari, A.; Vaziri, A.; Boudaoud, A. Wrinkling of Pressurized Elastic Shells. *Phys. Rev. Lett.* **2011**, *107*, 174301.

(24) Basheva, E. S.; Kralchevsky, P. A.; Christov, N. C.; Danov, K. D.; Stoyanov, S. D.; Blijdenstein, T. B. J.; Kim, H.-J.; Pelan, E. G.; Lips, A. Unique Properties of Bubbles and Foam Films Stabilized by HFBII Hydrophobin. *Langmuir* **2011**, *27*, 2382.

(25) King, H.; Schroll, R. D.; Davidovitch, B.; Menon, N. Elastic sheet on a liquid drop reveals wrinkling and crumpling as distinct symmetry-breaking instabilities. *Proc. Natl. Acad. Sci. U.S.A.* **2012**, *109*, 9716–9720.

(26) Landau, L.; Lifshitz, E. *Theory of Elasticity*; Butterworth-Heinemann: Oxford, 1986.

(27) This is a rough estimate, since this relation applies only to thin sheets of isotropic material, but the membranes at hand are evidently anisotropic.

(28) Aumaitre, E.; Knoche, S.; Cicuta, P.; Vella, D. Wrinkling in the deflation of elastic bubbles. *Eur. Phys. J. E: Soft Matter Biol. Phys.* **2013**, *36*, 22.

(29) Aumaitre, E. Viscoelastic properties of Hydrophobin layers. Ph.D. Thesis, University of Cambridge, 2012.
(30) Hakanpää, J.; Paananen, A.; Askolin, S.; Nakari-Setälä, T.; Parkkinen, T.; Penttilä, M.; Linder, M. B.; Rouvinen, J. Atomic resolution structure of the HFBII hydrophobin, a self-assembling amphiphile. *J. Biol. Chem.* **2004**, *279*, 534−539.
(31) Cox, A. R.; Cagnol, F.; Russell, A. B.; Izzard, M. J. Surface properties of class ii hydrophobins from Trichoderma reesei and influence on bubble stability. *Langmuir* **2007**, *23*, 7995−8002.
(32) Blijdenstein, T. B. J.; de Groot, P. W. N.; Stoyanov, S. D. On the link between foam coarsening and surface rheology: why hydrophobins are so different. *Soft Matter* **2010**, *6*, 1799.
(33) Ivanovska, I. L.; de Pablo, P. J.; Ibarra, B.; Sgalari, G.; MacKintosh, F. C.; Carrascosa, J. L.; Schmidt, C. F.; Wuite, G. J. L. Bacteriophage capsids: tough nanoshells with complex elastic properties. *Proc. Natl. Acad. Sci. U.S.A.* **2004**, *101*, 7600.
(34) Kisko, K.; Szilvay, G. R.; Vuorimaa, E.; Lemmetyinen, H.; Linder, M. B.; Torkkeli, M.; Serimaa, R. Self-assembled films of hydrophobin proteins HFBI and HFBII studied in situ at the air/water interface. *Langmuir* **2009**, *25*, 1612.
(35) Finken, R.; Seifert, U. Wrinkling of microcapsules in shear flow. *J. Phys.: Condens. Matter* **2006**, *18*, L185−L191.
(36) Walter, A.; Rehage, H.; Leonhard, H. Shear induced deformation of microcapsules: shape oscillations and membrane folding. *Colloids Surf., A* **2001**, *183−185*, 123−132.
(37) Stoer, J.; Bulirsch, R. *Introduction to numerical analysis*; Springer: New York, 2002.